Modulation of the Kuroshio Current on the M_2 Internal Tide Energetics at the Luzon Strait

ANZHOU CAO,[a] ZHENG GUO,[b] XU CHEN,[c] XINYU GUO,[d] AND JINBAO SONG[a]

[a] *State Key Laboratory of Ocean Sensing and Ocean College, Zhejiang University, Zhoushan, China*
[b] *Marine Science and Technology College, Zhejiang Ocean University, Zhoushan, China*
[c] *Key Laboratory of Physical Oceanography, Ocean University of China, Qingdao, China*
[d] *Center for Marine Environmental Studies, Ehime University, Matsuyama, Japan*

(Manuscript received 7 April 2025, in final form 23 February 2026, accepted 9 March 2026)

ABSTRACT: Previous studies have demonstrated that the internal tides (ITs) near the Luzon Strait (LS) are significantly modulated by the Kuroshio Current (KC). However, the modulation, particularly the contributions of the KC's velocity and stratification to the modulation, remains incompletely understood. Based on the interaction theory between subtidal motions and ITs, and 9-month numerical simulation results, this study investigates the KC's modulation on the M_2 IT energetics at the LS, with a focus on quantifying the contributions of the KC's velocity and stratification to the modulation. The KC directly modulates the IT energy budget through buoyancy production, shear production, and advection. Among them, the buoyancy production, associated with the KC's stratification, dominates over the shear production and advection, which are related to the KC's velocity. Furthermore, the KC influences the tidal conversion and energy flux of ITs by changing the pressure perturbation as well as barotropic and baroclinic tidal currents through nonlinear interaction with ITs. Sensitivity analysis indicates that the bottom pressure perturbation plays a more important role in the tidal conversion, whereas the baroclinic tidal currents are more crucial in the energy flux. Further analysis shows that the contributions of KC's velocity and stratification to the buoyancy and pressure perturbation are generally comparable. Moreover, the KC's velocity plays a more important role than the stratification in determining the phase speed of ITs, which leads to different energy flux patterns under different KC paths.

KEYWORDS: Internal waves; Ocean circulation; Ocean dynamics

1. Introduction

Internal tides (ITs) are internal waves with tidal frequencies, which are generated by barotropic tidal currents flowing over rough topographies in the stratified ocean. Hence, ITs are significant near the midocean ridges, continental slopes and shelves, as well as some small-scale topographies in the global ocean (Simmons et al. 2004; Niwa and Hibiya 2011, 2014; Müller et al. 2012; Müller 2013; Zhao 2019, 2024). As an important intermediate step in the ocean energy cascade, ITs play a crucial role in dissipating surface tidal energy and enhancing turbulent mixing in the ocean interior, which finally contributes to the maintenance of abyssal stratification (Munk and Wunsch 1998; Rudnick et al. 2003; Carter et al. 2012). Therefore, investigating the generation, propagation, and dissipation of ITs is of great importance.

The subtidal motions in the ocean, such as the large-scale circulation and mesoscale eddies, are found to modulate the tidal conversion, energy flux, and incoherence of ITs. Based on moored observations, Löb et al. (2020) showed that the passing of two eddies caused a pronounced damping of in situ energy flux of ITs to the south of the Azores in the Atlantic Ocean. Through analyzing 24-yr satellite altimetry sea surface height data, Zhao and Qiu (2023) studied the seasonal variation of the M_2 ITs radiated from the Luzon Strait (LS) and indicated that the seasonal seesaw of IT characteristics here is mainly determined by the Kuroshio Current (KC) and ocean stratification. These observational studies provide direct evidence for the modulation of ITs by large-scale circulation and mesoscale eddies, which is further demonstrated by numerical studies. By using a three-dimensional model with idealized settings, Jan et al. (2012) pointed out that the KC enhances (weakens) the energy flux of semidiurnal (diurnal) ITs radiated to the South China Sea. Based on a 1-yr numerical simulation of the M_2 ITs and subtidal circulation in the Philippine Sea, Kerry et al. (2014a) showed that the subtidal circulation (especially the KC) significantly modulates the generation and propagation of the M_2 ITs, of which the tidal conversion at the LS varies from 13 to 20 GW and the energy fluxes radiated from the LS exhibit temporal and spatial variations. At the same time, the IT-induced turbulent mixing and incoherence of ITs are also influenced by the subtidal circulation (Kerry et al. 2014b, 2016). Xu et al. (2021) and Cao et al. (2022) further pointed out that when the KC takes different paths, its effects on the energetics and incoherence of ITs at the LS are different. Buijsman et al. (2017) studied the incoherence of semidiurnal ITs in the equatorial Pacific Ocean and revealed that the temporal variability of vertically sheared background flow associated with jets and tropical instability waves is an important cause. Moreover, Dunphy and Lamb (2014) found that when mode-1 ITs pass through a barotropic eddy, hot and cold spots of energy fluxes are produced in beam-like patterns. Guo et al. (2023) showed that along the main propagation path of the M_2 ITs in the South China Sea, the anticyclonic eddy and cyclonic eddy cause northward and southward refractions of the M_2 ITs, respectively.

The modulation of ITs by these subtidal motions is attributed to the low-frequency currents and stratification associated

Corresponding author: Anzhou Cao, caoanzhou@zju.edu.cn

DOI: 10.1175/JPO-D-25-0083.1

with them (e.g., Kerry et al. 2014a; Kelly and Lermusiaux 2016; Buijsman et al. 2017; Xu et al. 2021; Cao et al. 2022, 2023; Guo et al. 2023). First, ocean stratification is an important factor in the generation of ITs (e.g., Bell 1975; Smith and Young 2003). When subtidal motions appear at the generation site of ITs, they can change the local stratification and hence the local tidal conversion. For example, the shelfbreak front in the Middle Atlantic Bight region with horizontally variable stratification decreases the local IT generation by 10% (Kelly and Lermusiaux 2016). Second, through the interaction between ITs and subtidal motions, the pressure perturbation and barotropic tidal currents are changed, which also influence the local tidal conversion (Kerry et al. 2014a; Cao et al. 2023). Third, according to the Taylor–Goldstein equation, both the low-frequency currents and stratification associated with subtidal motions can modulate the eigenspeed of ITs, which would further influence the propagation of ITs, causing scattering, refraction, and incoherence of ITs (Kelly and Lermusiaux 2016; Buijsman et al. 2017; Duda et al. 2018; Savage et al. 2020; Cao et al. 2022; Guo et al. 2023).

The LS, composed of two meridional ridges, is a typical generation site of ITs in the global ocean (e.g., Alford et al. 2011, 2015). Near the LS, the KC, one of the most intense western boundary currents in the global ocean, can take three different paths (Nan et al. 2011): The looping KC enters the South China Sea in the middle and outflows in the northern part of the LS, causing an anticyclonic current loop; the leaking KC bends anticyclonically in the LS with a portion leaking into the South China Sea; and the leaping KC flows across the LS and continues northward along the east coast of Taiwan Island, which intrudes the least into the South China Sea among the three paths. Previous studies have demonstrated that the KC has considerable impacts on the ITs at the LS (e.g., Kerry et al. 2014a,b, 2016; Xu et al. 2021; Cao et al. 2022). However, the modulation of the KC on the IT energetics at the LS, especially the contributions of the KC's velocity and stratification to the modulation, is not fully understood (Zhao and Qiu 2023). Therefore, a three-dimensional numerical model is developed in this study to simultaneously simulate the M_2 ITs and the KC near the LS. Based on the interaction theory between subtidal motions and ITs and numerical simulation results, the contributions of KC's velocity and stratification to the modulation are evaluated. The remainder of the paper is organized as follows. The interaction theory between subtidal motions and ITs is introduced in section 2. The model configurations and data analysis methods are displayed in section 3. The main results are shown in section 4. Finally, a discussion and a summary complete the paper in section 5.

2. Theory frameworks

The governing equations for the inviscid motion in the ocean are

$$\frac{\partial \mathbf{u}}{\partial t} + (\mathbf{u}\cdot\nabla)\mathbf{u} + f\hat{\mathbf{k}}\times\mathbf{u} = -\frac{1}{\rho}\nabla p + b\hat{\mathbf{k}}, \tag{1}$$

$$\frac{\partial b}{\partial t} + \mathbf{u}\cdot\nabla b = 0, \tag{2}$$

$$\nabla\cdot\mathbf{u} = 0, \tag{3}$$

where $\mathbf{u} = (u, v, w)$ is the velocity vector, t is the time, $\nabla = (\partial/\partial x, \partial/\partial y, \partial/\partial z)$ is the gradient operator, f is the Coriolis frequency, $\hat{\mathbf{k}}$ is the unit vector in the vertical direction, ρ is the density, p is the pressure, and

$$b = -g(\rho - \rho_0)/\rho_0 \tag{4}$$

is the buoyancy, where g is the gravitational acceleration and ρ_0 is the reference density. Assuming that there simultaneously exist subtidal motions and ITs in the system, the density can be expressed as

$$\rho(x, y, z, t) = \rho_0 + \overline{\rho}(x, y, z, t) + \rho'(x, y, z, t), \tag{5}$$

where $\overline{\rho}$ and ρ' are the density perturbations associated with subtidal motions and ITs, respectively. According to the hydrostatic approximation

$$\partial p/\partial z = -\rho g, \tag{6}$$

the pressure becomes

$$p(x, y, z, t) = p_0(z) + \overline{p}(x, y, z, t) + p'(x, y, z, t). \tag{7}$$

The velocity and buoyancy can be also divided into two parts:

$$\mathbf{u}(x, y, z, t) = \overline{\mathbf{u}}(x, y, z, t) + \mathbf{u}'(x, y, z, t), \tag{8}$$

$$b(x, y, z, t) = \overline{b}(x, y, z, t) + b'(x, y, z, t), \tag{9}$$

corresponding to the subtidal motions (denoted by the overbar) and ITs (denoted by the prime), respectively. Introducing Eqs. (5)–(9) into Eqs. (1)–(3), one can get the equations for the subtidal motions and ITs, respectively (Kelly and Lermusiaux 2016).

As the focus of this study is the modulation of ITs by the KC, we only focus on the equations for ITs under the Boussinesq approximation, which are

$$\frac{\partial \mathbf{u}'}{\partial t} + (\overline{\mathbf{u}}\cdot\nabla)\mathbf{u}' + (\mathbf{u}'\cdot\nabla)\overline{\mathbf{u}} + f\hat{\mathbf{k}}\times\mathbf{u}' = -\frac{1}{\rho_0}\nabla p' + b'\hat{\mathbf{k}}, \tag{10}$$

$$\frac{\partial b'}{\partial t} + \overline{\mathbf{u}}\cdot\nabla b' + \mathbf{u}'\cdot\nabla\overline{b} = 0, \tag{11}$$

$$\nabla\cdot\mathbf{u}' = 0. \tag{12}$$

Note that the slowly varying buoyancy frequency is $N = \sqrt{\partial\overline{b}/\partial z}$. Multiplying Eq. (10) by $\rho_0\mathbf{u}'$ and Eq. (11) by $\rho_0 b'/N^2$, neglecting the terms that involve the derivative of N (Hazewinkel and Winters 2011; Kelly and Lermusiaux 2016; Wang et al. 2021), summing them up, and integrating in the vertical direction, we get the IT energy equation:

$$\frac{\partial E}{\partial t} = -\nabla_H\cdot\mathbf{F} + A + P_S + P_B, \tag{13}$$

where

$$E = \int_{-h}^{0}\frac{1}{2}\rho_0\left(u'^2 + v'^2 + w'^2 + \frac{b'^2}{N^2}\right)dz, \tag{14}$$

$$\mathbf{F} = \int_{-h}^{0} p'\mathbf{u}'_H dz, \tag{15}$$

$$A = \int_{-h}^{0} -\rho_0 \nabla\cdot(\overline{\mathbf{u}}E)dz = \int_{-h}^{0} -\rho_0\left[\mathbf{u}'\cdot(\overline{\mathbf{u}}\cdot\nabla)\mathbf{u}' + \frac{b'}{N^2}(\overline{\mathbf{u}}\cdot\nabla b')\right]dz, \tag{16}$$

$$P_S = \int_{-h}^{0} -\rho_0\mathbf{u}'\cdot(\mathbf{u}'\cdot\nabla)\overline{\mathbf{u}}dz, \tag{17}$$

$$P_B = \int_{-h}^{0} -\rho_0\frac{b'}{N^2}(\mathbf{u}'\cdot\nabla\overline{b})dz, \tag{18}$$

in which h is the water depth and the subscript H denotes the horizontal component. Note that the continuity equations for both the subtidal motions and ITs ($\nabla\cdot\overline{\mathbf{u}} = 0$ and $\nabla\cdot\mathbf{u}' = 0$) have been used in the above derivation. In Eq. (13), E is the total IT energy containing both kinetic energy and available potential energy, $\mathbf{F}$ is the IT energy flux, A is the IT energy advection caused by the subtidal motions, and P_S and P_B are the IT energy production terms related to the shear and stratification of the subtidal motions (Kelly and Lermusiaux 2016), which are named as shear production and buoyancy production, respectively.

Equation (13) is not the complete form of IT energy budget, as the generation and dissipation of ITs are not considered in Eqs. (10)–(12). Therefore, the complete form of IT energy budget contains two more terms, i.e., the tidal conversion C and dissipation D, as shown in Eq. (19):

$$\frac{\partial E}{\partial t} = C - \nabla_H\cdot\mathbf{F} + A + P_S + P_B - D. \tag{19}$$

The tidal conversion is calculated as

$$C(x, y, t) = p'(x, y, -h, t)w^{\mathrm{bt}}(x, y, -h, t), \tag{20}$$

where

$$w^{\mathrm{bt}}(x, y, -h, t) = -u^{\mathrm{bt}}(x, y, t)\frac{\partial h(x, y)}{\partial x} - v^{\mathrm{bt}}(x, y, t)\frac{\partial h(x, y)}{\partial y}, \tag{21}$$

in which u^{bt}, v^{bt}, and w^{bt} are the horizontal and vertical components of barotropic tidal currents. According to previous studies (e.g., Kerry et al. 2014a; Xu et al. 2021; Cao et al. 2023), the dissipation is calculated as the residual of other terms in Eq. (19).

3. Data and methods

a. Model configurations

The Regional Ocean Modeling System (ROMS) under the framework of the Coastal and Regional Ocean Community (CROCO) model (version 1.0; https://www.croco-ocean.org/download/) is adopted to simultaneously simulate the M_2 ITs and the KC near the LS (Fig. 1) from 1 July 2010 to 30 April 2011.

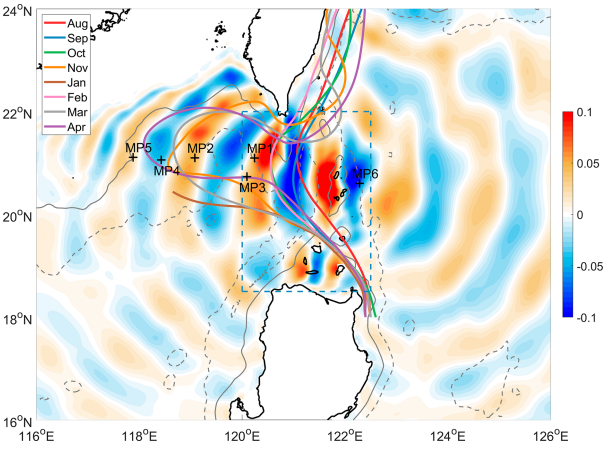

FIG. 1. The study domain as well as the simulated KC and ITs. The shading indicates the sea surface height induced by the M_2 ITs (m). The colored curves denote the major axes of the KC in different months. The gray solid and dashed curves represent the 1000- and 3000-m isobaths. The dashed blue box indicates the LS. The black pluses denote the mooring locations in Cao et al. (2017).

The simulated domain (115.5°–126.5°E and 15.5°–24.5°N), horizontal resolution (1/20°), sigma layer (30 layers in the vertical direction), and sponge layer (0.5° at four open boundaries) settings as well as the parameterization schemes are the same as Cao et al. (2023). The Oregon State University TOPEX/Poseidon Global Inverse Solution tidal model 7 (TPXO7; Egbert and Erofeeva 2002) provides the barotropic tidal forcing for the M_2 constituent. The Hybrid Coordinate Ocean Model (HYCOM) reanalysis data provide the initial and boundary conditions (https://tds.hycom.org/thredds/catalogs/GLBv0.08/expt_53.X.html). The surface forcing is obtained from the Climate Forecast System Reanalysis data (https://tds.hycom.org/thredds/catalog/datasets/force/ncep_cfsr/netcdf/catalog.html; https://tds.hycom.org/thredds/catalog/datasets/force/ncep_cfsv2/netcdf/catalog.html). The simulated results are output every 1 h.

b. Data analysis methods

To ensure that the simulated KC and ITs are sufficiently developed, the simulated results in July 2010 are discarded. In other words, the 9-month (from August 2010 to April 2011) simulation results are used for the following analysis. Thereafter, low-pass filtering with a cutoff frequency of 0.5 cpd is conducted to extract the density and velocity ($\overline{\rho}$ and $\overline{\mathbf{u}}$) associated with the KC (Cao et al. 2022). The monthly mean simulated surface currents are compared with the corresponding satellite-observed surface geostrophic currents to validate the reasonability of simulation and determine the detailed path of the KC (Fig. 1), which will be shown in section 4a. The density and velocity (ρ' and $\mathbf{u}'$) associated with the M_2 ITs are extracted through bandpass filtering with a cutoff frequency of [1.73, 2.13] cpd (e.g., Zhao et al. 2010; Cao et al. 2025). To improve the computing efficiency, the filtering is performed with a 50-day sliding window. To avoid the endpoint effect of the filtering, the first and last 10-day filtered results in each 50-day sliding window are discarded. Therefore, we obtain the filtered

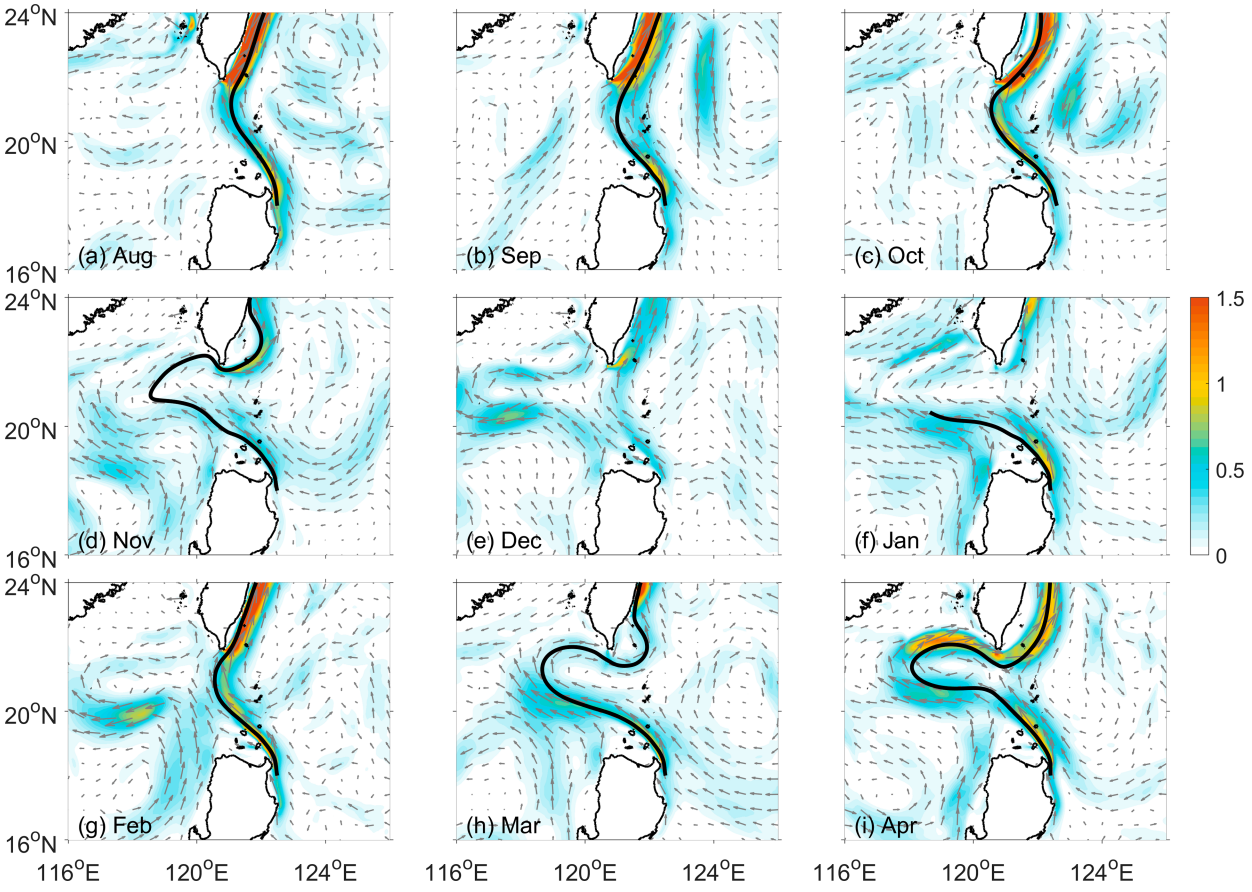

FIG. 2. Monthly mean simulated surface currents (magnitude: shading; direction: quivers). The black curves denote the major axes of the KC in different months.

results of the KC and M_2 ITs from 11 August 2010 to 20 April 2011 for further analysis. Using $\overline{\rho}$ and ρ', the buoyancy ($\overline{b}$ and b') and pressure ($\overline{p}$ and p') terms are calculated via Eqs. (4) and (6). Finally, all the terms in the IT energy budget [Eq. (19)] are computed, and the contributions of KC's velocity and stratification to the modulation of ITs are evaluated. Moreover, harmonic analysis (Pawlowicz et al. 2002) is conducted for the 9-month velocities at the six moorings (Fig. 1) to validate the reasonability of simulated ITs through a comparison with observations, which will be shown in section 4a.

4. Results

a. *Validation of simulated results*

The simulated results are validated before investigating the modulation of the M_2 ITs by the KC. Figure 2 shows the monthly mean simulated surface currents, and Fig. 3 displays the monthly mean satellite-observed surface geostrophic currents obtained from the Copernicus Marine Data (https://data.marine.copernicus.eu/product/SEALEVEL_GLO_PHY_CLIMATE_L4_MY_008_057/services). Overall, the simulated KC demonstrates a general consistency with the observed KC in most months. Specifically, the model successfully reproduces the characteristic path of the KC: a leaping path in August–October 2010 and February 2011, a looping path in November 2010 and March–April 2011, and a leaking path in January 2011. However, some discrepancies are noted, particularly in December 2010 when the simulated KC exhibited a complicated pattern that differs from an obvious looping path observed by the satellite. This deviation can be attributed to the absence of data assimilation in the numerical simulation, which inherently limits the model's ability to fully replicate observed conditions (Kerry et al. 2014a). Consequently, we refrain from assigning a specific path for the simulated KC in December 2010 in the subsequent analysis. Nevertheless, given the overall agreement between the simulated and observed KC paths in most months, we believe that the simulation results provide a reasonable representation of the KC.

The accuracy of simulated M_2 ITs is validated through a comparison with in situ observations collected at six moorings near the LS (Fig. 1; Cao et al. 2017). As illustrated in Fig. 4, the model demonstrates remarkable consistency with the observations, particularly in reproducing the vertical structure of the M_2 ITs. Quantitative analysis reveals that the depth-averaged mean absolute errors of the amplitude of the M_2 zonal velocity at the six moorings are 0.038, 0.023, 0.025, 0.012, 0.024, and 0.038 m s^{-1}, respectively, all falling within a low error range.

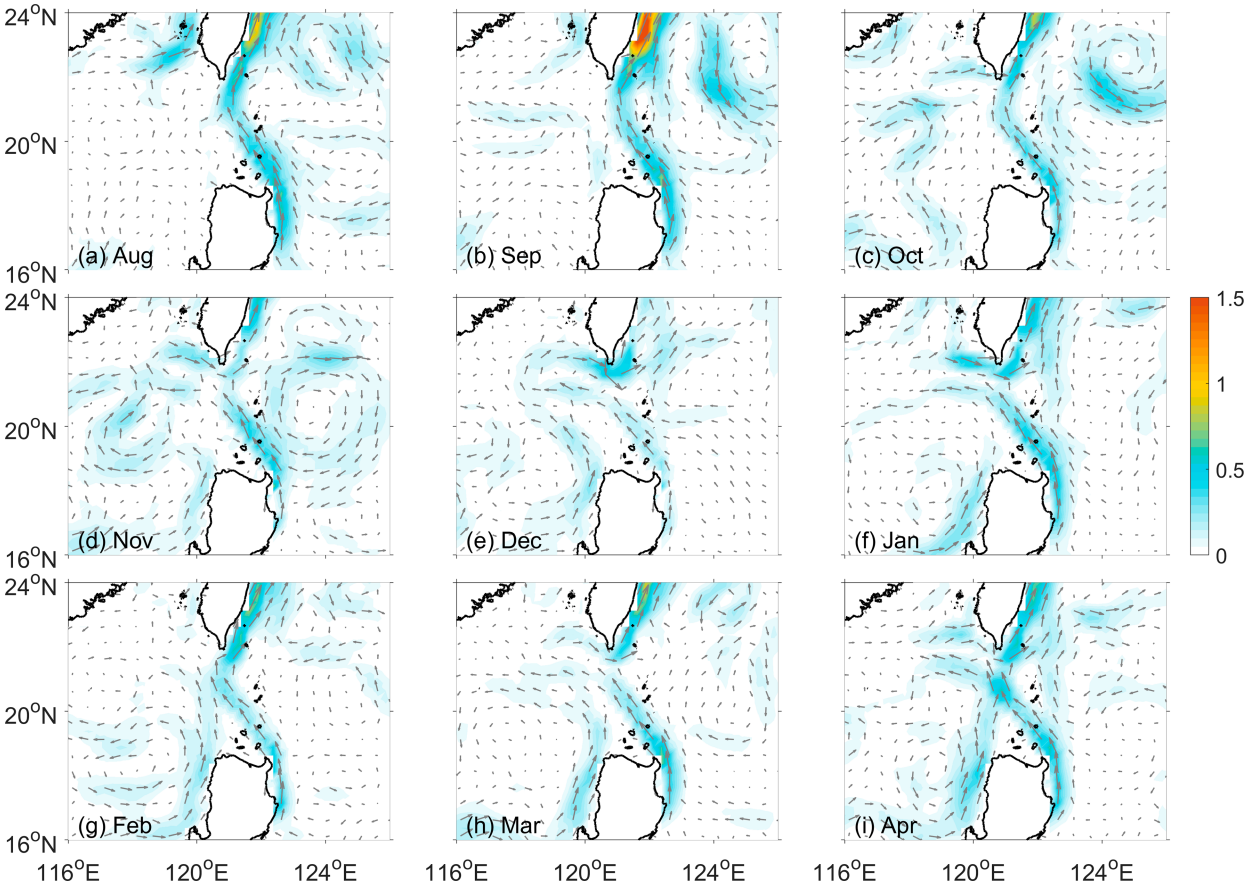

FIG. 3. Monthly mean satellite-observed surface geostrophic currents (magnitude: shading; direction: quivers).

Moreover, the simulated sea surface height induced by the M_2 ITs (Fig. 1) shares a similar pattern as that obtained from long-term satellite observations (Zhao 2019). These validation results strongly support the reliability and accuracy of the simulated M_2 ITs in this study.

b. *Influence of the KC on the IT energy budget*

As the aim of this study is to investigate the modulation of the KC on the M_2 ITs at the LS (Fig. 1), attention is first paid to the IT energy budget [Eq. (19)]. Figure 5 shows the monthly values of all the terms in the IT energy budget. Due to the fact that the tidal conversion, which represents the energy transfer from barotropic tides to ITs, serves as the major source term in Eq. (19), it is undoubtedly the dominant component in the IT energy budget. In our simulation, the monthly tidal conversion ranges from 19.5 to 21.8 GW (Fig. 5a). This value is a little larger than that estimated by Kerry et al. (2014a) but remains reasonable because a higher resolution is used in the CROCO

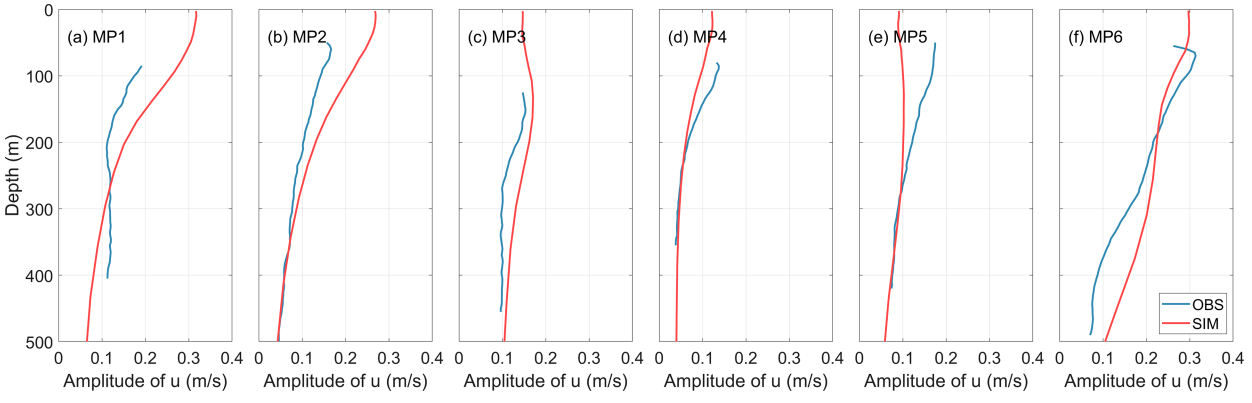

FIG. 4. Comparison of the amplitude of the M_2 zonal velocity between simulation (red) and observation (blue) at the six moorings.

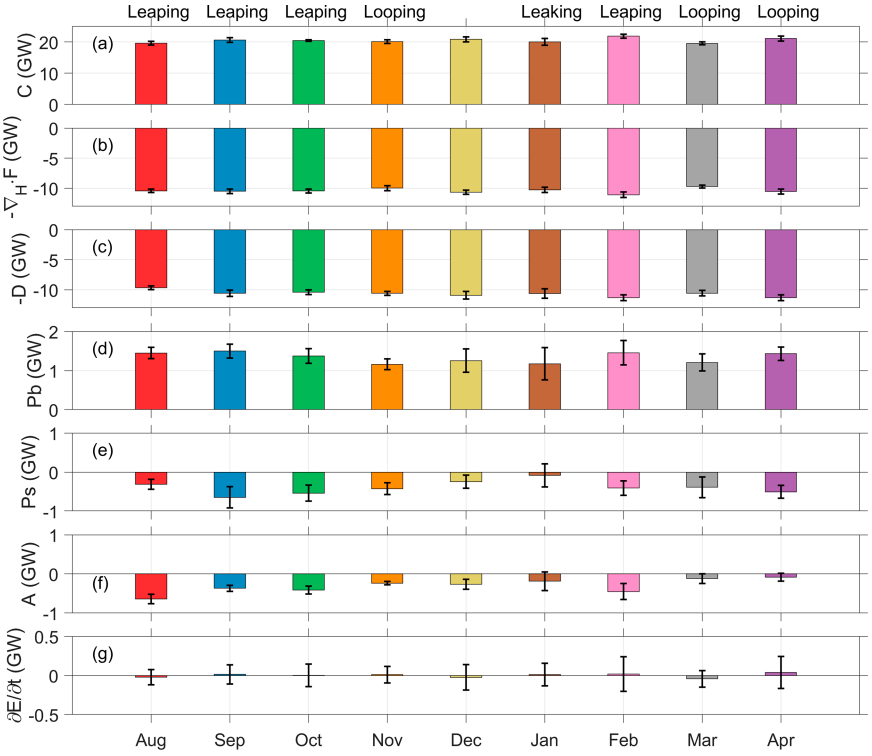

FIG. 5. Monthly averaged (a) tidal conversion, (b) energy flux divergence, (c) dissipation, (d) buoyancy production, (e) shear production, (f) advection, and (g) partial derivative of energy of the M_2 ITs integrated at the LS from August 2010 to April 2011. The standard deviation of 25-h segment (nearly two M_2 periods) is shown as black error bar. The corresponding path of the KC is labeled at the top of the figure.

and bandpass filtering is adopted to extract the M_2 IT signals in this study. The M_2 ITs generated at the LS mainly propagate westward into the South China Sea and eastward into the Philippine Sea, resulting in remarkable values of energy flux divergence near the LS (Fig. 5b), which are approximately one-half of the tidal conversion. Compared to the tidal conversion and energy flux divergence, the buoyancy production, shear production, and advection related to the KC are one order of magnitude smaller (Figs. 5d–f), and the derivative of energy with respect to time is close to 0 (Fig. 5g), which can be neglected (Kelly and Lermusiaux 2016). Hence, the IT energy budget is mainly balanced by the tidal conversion, energy flux divergence, and local dissipation (Fig. 5c), even under the influence of the KC. The monthly local dissipation efficiency ($q = D/C$) at the LS ranges from 0.49 to 0.54, which is comparable to those reported in previous studies (e.g., Xu et al. 2021; Cao et al. 2023).

We then focus on the buoyancy production, shear production, and advection, which are related to the KC's velocity and stratification [Eqs. (16)–(18)]. It is important to note that the buoyancy production is directly related to the KC's stratification $\overline{b}$. Both the sustained inflow (caused by the persistent intrusion and maintaining a locally stratified water column) and enhanced buoyancy gradient (caused by the local steepening of isopycnals) of the KC can influence the buoyancy production because the former influences N^2 and the latter changes $\nabla\overline{b}$. In contrast, the shear production and advection are mainly related to the KC's velocity $\overline{\mathbf{u}}$. Overall, the buoyancy production remains positive in the 9 months (Fig. 5d), whereas the shear production and advection are negative (Figs. 5e,f). According to Eq. (19), a positive (negative) value at the right-hand side indicates an increasing (decreasing) trend of the IT energy. Consequently, the buoyancy production has the potential to enhance the IT energy, whereas the shear production and advection tend to reduce it. On the other hand, the magnitude of buoyancy production exceeds that of both shear production and advection, as well as their combined total, regardless of the path taken by the KC. In the 9 months, the values of $A + P_S + P_B$ vary from 0.42 to 0.90 GW (Fig. 6). This result suggests that the buoyancy production dominates over the shear production and advection in the IT energy budget. Moreover, it is found that the values of $A + P_S + P_B$ under the looping and leaking KC are generally larger than those under the leaping KC, confirming again that the KC exerts path-dependent modulation on the M_2 IT energetics near the LS. We speculate that the smaller values of $A + P_S + P_B$ under the leaping KC is related to its least intrusion into the South China Sea.

c. *Influences of the KC on the tidal conversion*

In addition to directly influence the IT energy budget through buoyancy production, shear production, and advection,

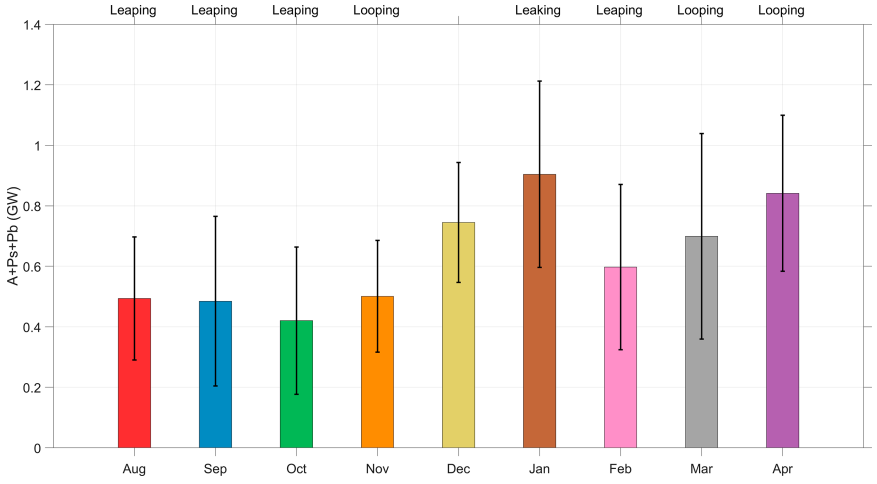

FIG. 6. Monthly averaged value of $A + P_S + P_B$. The standard deviation of 25-h segment (nearly two M_2 periods) is shown as black error bar. The corresponding path of the KC is labeled at the top of the figure.

the KC can also modulate the tidal conversion and energy flux of ITs. First, the KC's velocity $\overline{\mathbf{u}}$ and stratification $\overline{b}$ can modulate the buoyancy of the M_2 ITs [Eq. (11)], which further influences the pressure perturbation of the M_2 ITs, because

$$\frac{\partial p'}{\partial z} = \rho_0 b', \tag{22}$$

according to Eqs. (4)–(7). Second, the KC's velocity $\overline{\mathbf{u}}$ can affect the baroclinic tidal currents according to Eq. (10) and barotropic tidal currents according to

$$\frac{\partial \mathbf{u}_H^{\mathrm{bt}}}{\partial t} + (\overline{\mathbf{u}}_H \cdot \nabla_H)\mathbf{u}_H^{\mathrm{bt}} + (\mathbf{u}_H^{\mathrm{bt}} \cdot \nabla_H)\overline{\mathbf{u}}_H + f\hat{\mathbf{k}} \times \mathbf{u}_H^{\mathrm{bt}} = -g\nabla_H \eta. \tag{23}$$

In other words, the KC's velocity can modulate the tidal conversion (energy flux) through both the pressure perturbation and barotropic (baroclinic) tidal currents, whereas the KC's stratification can affect the pressure perturbation [Eqs. (15) and (20)].

We then estimate the sensitivities of tidal conversion following Kerry et al. (2014a) and Cao et al. (2023). According to Eq. (20), the tidal period-averaged conversion rate can be written as

$$C(x, y) = \frac{1}{2}P(x, y, -h)W(x, y, -h)\cos[\theta_P(x, y, -h) - \theta_W(x, y, -h)], \tag{24}$$

where P, W, θ_P, and θ_W are the amplitudes and phases of bottom pressure perturbation and vertical barotropic velocity, respectively. Therefore, it is easy to obtain the sensitivities of conversion rate with respect to P, W, and $\Delta\theta = \theta_P - \theta_W$:

$$\Delta C_P = \frac{\partial C}{\partial P}\sigma_P = \frac{1}{2}W\cos\Delta\theta\sigma_P, \tag{25}$$

$$\Delta C_W = \frac{\partial C}{\partial W}\sigma_W = \frac{1}{2}P\cos\Delta\theta\sigma_W, \tag{26}$$

$$\Delta C_\theta = \frac{\partial C}{\partial \Delta\theta}\sigma_{\Delta\theta} = -\frac{1}{2}PW\sin\Delta\theta\sigma_{\Delta\theta}, \tag{27}$$

where σ_P, σ_W, and $\sigma_{\Delta\theta}$ are the standard deviations of P, W, and $\Delta\theta$, respectively. In this study, we conduct harmonic analysis for each 25-h segment to obtain P, W, and $\Delta\theta$ and thereafter calculate their time-averaged values and standard deviations σ_P, σ_W, and $\sigma_{\Delta\theta}$ (Fig. 7). As shown, the spatial patterns of P, $\Delta\theta$, σ_P, and $\sigma_{\Delta\theta}$ are generally consistent with those in Kerry et al. (2014a), but the detailed values of them slightly differ due to the different model settings.

Figure 8 shows the time series and spatial patterns of tidal conversion sensitivities ΔC_P, ΔC_W, and ΔC_θ. It is clearly shown that ΔC_P dominates over ΔC_W for the whole simulation, with the former 2–3 times larger than the latter, suggesting that the bottom pressure perturbation plays a more important role than the bottom vertical barotropic velocity in the tidal conversion. The ΔC_θ exhibits a value intermediate between ΔC_P and ΔC_W, suggesting that the phase difference between bottom pressure perturbation and vertical barotropic velocity is also an important factor for the tidal conversion at the LS. It should be noted that the value of ΔC_P in this study is comparable to that estimated by Kerry et al. (2014a), whereas the value of ΔC_θ is smaller than that in Kerry et al. (2014a). We speculate that the cause for such difference is related to the different simulation domain between this study and Kerry et al. (2014a). In Kerry et al. (2014a), the simulation domain contained the Mariana Island Arc, and the M_2 ITs at the LS are affected by those radiated from the Mariana Island Arc (Kerry et al. 2013). As demonstrated by Kelly and Nash (2010), the remotely generated shoaling ITs can change the local pressure perturbation and modulate the tidal conversion.

We further examine the contributions of KC's velocity and stratification to the pressure perturbation of ITs by calculating the nonlinear terms in Eq. (11), i.e., $\overline{u}\partial b'/\partial x$, $\overline{v}\partial b'/\partial y$, $\overline{w}\partial b'/\partial z$, $u'\partial\overline{b}/\partial x$, $v'\partial\overline{b}/\partial y$, and $w'\partial\overline{b}/\partial z$, according to the relation between

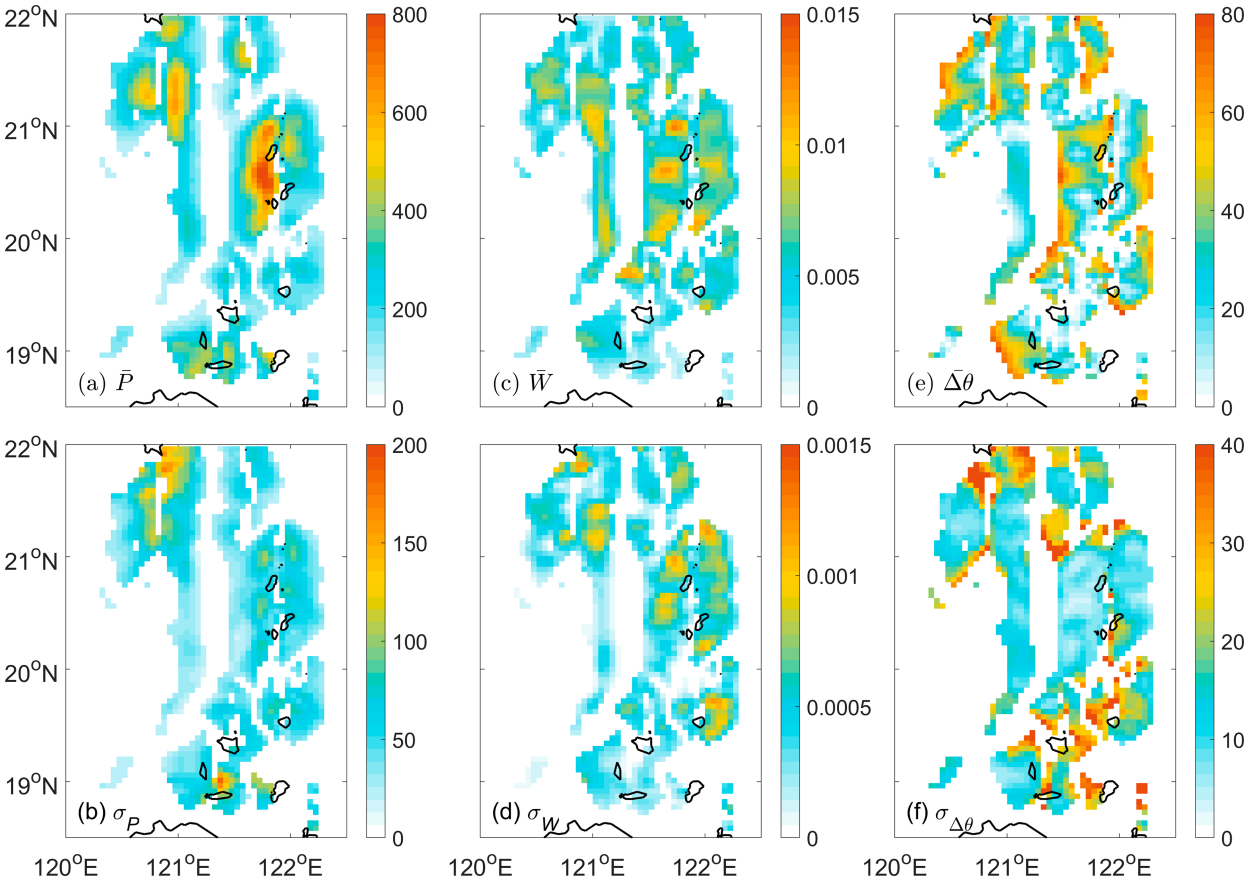

FIG. 7. Spatial distributions of time-averaged (a) P (Pa), (c) W (m s^{-1}), and (e) $\Delta\theta$ (°) as well as their standard deviations (b) σ_P (Pa), (d) σ_W (m s^{-1}), and (f) $\sigma_{\Delta\theta}$ (°). Note that only the results at grids where the local tidal conversion rate exceeds 0.2 W m^{-2} are shown.

pressure perturbation and buoyancy of ITs [Eq. (22)]. Note that since $\overline{b}(x, y, z, t)$ is derived from $\overline{\rho}(x, y, z, t)$ which is obtained through low-pass filtering (section 3a), it incorporates the contribution of oceanic background stratification that is independent of the KC. Hence, when calculating $w'\partial\overline{b}/\partial z$, the contribution of oceanic background stratification is removed by subtracting the 9-month-averaged $\overline{\overline{b}}(z) = \overline{b}(x, y, z, t)$ from $\overline{b}(x, y, z, t)$. As shown in Figs. 9 and 10a, with the contribution of oceanic background stratification, $w'\partial\overline{b}/\partial z$ is at least one order of magnitude larger than the other five nonlinear terms in Eq. (11), whereas removing the contribution of oceanic background stratification, $w'\partial\overline{b}/\partial z$ is on the same level as $\overline{u}\partial b'/\partial x$ and $\overline{v}\partial b'/\partial y$ but still larger than the other three nonlinear terms. Consequently, the values of $\overline{\mathbf{u}}\cdot\nabla b'$ and $\mathbf{u}'\cdot\nabla\overline{b}$ are comparable (Fig. 10b) in the 9 months. This result suggests that the contributions of KC's velocity and stratification to the buoyancy and hence pressure perturbation of ITs are generally comparable. At the same time, $\overline{\mathbf{u}}\cdot\nabla b'$ and $\mathbf{u}'\cdot\nabla\overline{b}$ do not show a significant correlation with the KC path. Moreover, larger values of $\overline{u}\partial b'/\partial x$, $\overline{v}\partial b'/\partial y$, and $w'\partial\overline{b}/\partial z$ mainly appear on the east ridge and north part of the west ridge of the LS (Fig. 10), indicating that the interaction between the KC and ITs mainly occurs here.

d. *Influences of the KC on the energy flux*

Similar to the tidal conversion, the sensitivities of energy flux are analyzed. According to Eq. (15), the tidal-period-averaged energy flux can be written as

$$F^x(x, y) = \int_{-h}^{0} \frac{1}{2} P(x, y, z) U(x, y, z) \cos[\theta_P(x, y, z) - \theta_U(x, y, z)]dz, \tag{28}$$

$$F^y(x, y) = \int_{-h}^{0} \frac{1}{2} P(x, y, z) V(x, y, z) \cos[\theta_P(x, y, z) - \theta_V(x, y, z)]dz, \tag{29}$$

where U, V, θ_U, and θ_V are the amplitudes and phases of zonal and meridional baroclinic tidal currents, respectively. Given that the M_2 ITs generated at the LS primarily propagate westward into the South China Sea and eastward into the Philippine Sea, we mainly focus on the sensitivities of zonal energy flux along the east and west boundaries of the LS. The sensitivities of zonal energy flux to pressure perturbation, zonal baroclinic tidal currents, and their phase difference are

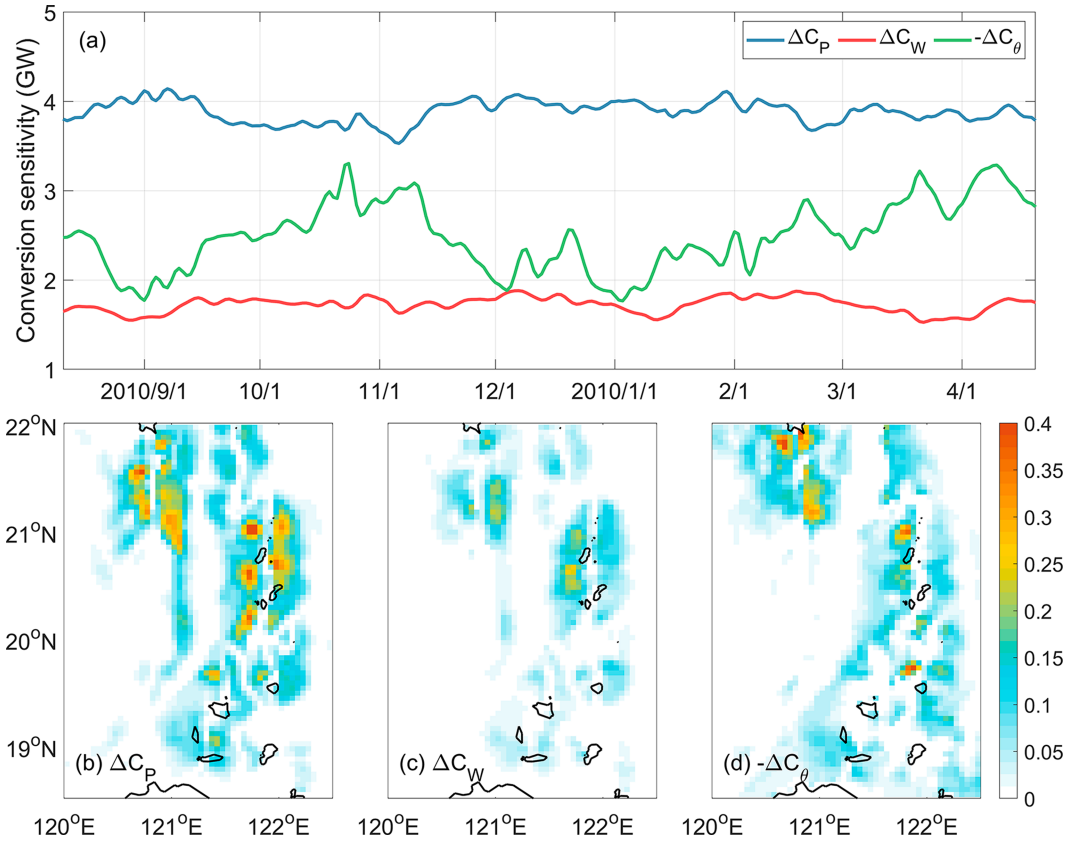

FIG. 8. (a) Domain-integrated tidal conversion sensitivities to the bottom pressure perturbation (ΔC_P; blue), vertical barotropic velocity (ΔC_W; red), and their phase difference ($-\Delta C_\theta$; green) at the LS. Spatial patterns of tidal conversion sensitivities (b) ΔC_P, (c) ΔC_W, and (d) $-\Delta C_\theta$ (W m^{-2}).

$$\Delta F_P^x = \frac{\partial F^x}{\partial P}\sigma_P = \int_{-h}^{0}\frac{1}{2}U\cos\Delta\theta_2\sigma_P dz, \tag{30}$$

$$\Delta F_U^x = \frac{\partial F^x}{\partial U}\sigma_U = \int_{-h}^{0}\frac{1}{2}P\cos\Delta\theta_2\sigma_U dz, \tag{31}$$

$$\Delta F_\theta^x = \frac{\partial F^x}{\partial \Delta\theta_2}\sigma_{\Delta\theta_2} = -\int_{-h}^{0}\frac{1}{2}PU\sin\Delta\theta_2\sigma_{\Delta\theta_2} dz, \tag{32}$$

where $\Delta\theta_2 = \theta_P - \theta_U$ and σ_U and $\sigma_{\Delta\theta_2}$ are the standard deviations of U and $\Delta\theta_2$, respectively. Figure 11 shows the zonal energy flux sensitivities ΔF_P^x, ΔF_U^x, and ΔF_θ^x integrated along the west and east boundaries of the LS. Since F^x has different signs at the two boundaries, ΔF_P^x, ΔF_U^x, and ΔF_θ^x also exhibit different signs. Therefore, their magnitude is shown in Fig. 11 for comparison. As shown, along both boundaries of the LS, ΔF_U^x dominates over ΔF_P^x at most of the time, suggesting that the zonal baroclinic tidal currents play a more important role than the pressure perturbation in the M_2 energy flux radiated westward and eastward from the LS. The ΔF_θ^x is also smaller than ΔF_U^x, but it is sometimes larger than ΔF_P^x. Moreover, it is found that both ΔF_U^x and ΔF_P^x along the west boundary of the LS (Fig. 11a) are larger than those along the east boundary (Fig. 11b). This result suggests that the westward energy flux radiated from the LS into the South China Sea is more variable than the eastward energy flux into the Philippine Sea under the influence of the KC.

The KC also modulates the M_2 energy flux pattern, which is path dependent. Figures 12a and 12b show the M_2 energy fluxes in September 2010 (leaping KC) and March 2011 (looping KC) as examples. In the 2 months, the M_2 energy fluxes exhibit apparently different patterns, especially in the South China Sea. Under the influence of the leaping KC, intense M_2 energy flux mainly appears at the middle of the LS and propagates westward, and the northwestward M_2 energy flux at the north part of the LS is a little weaker (Fig. 12a). However, under the looping KC, the northwestward M_2 energy flux radiated from the north part of the LS is significantly enhanced, which is stronger than the westward M_2 energy flux radiated from the middle of the LS (Fig. 12b). Moreover, the M_2 energy flux radiated from the north part of the LS refracts more northward under the looping KC than under the leaping KC. In contrast, the M_2 energy flux patterns in the Philippine Sea are similar under the different KC paths.

The different M_2 energy flux patterns in the South China Sea induced by the leaping and looping KC can be generally reproduced by the ray-tracing model developed by Duda et al. (2018), of which the results are indicated by black curves in

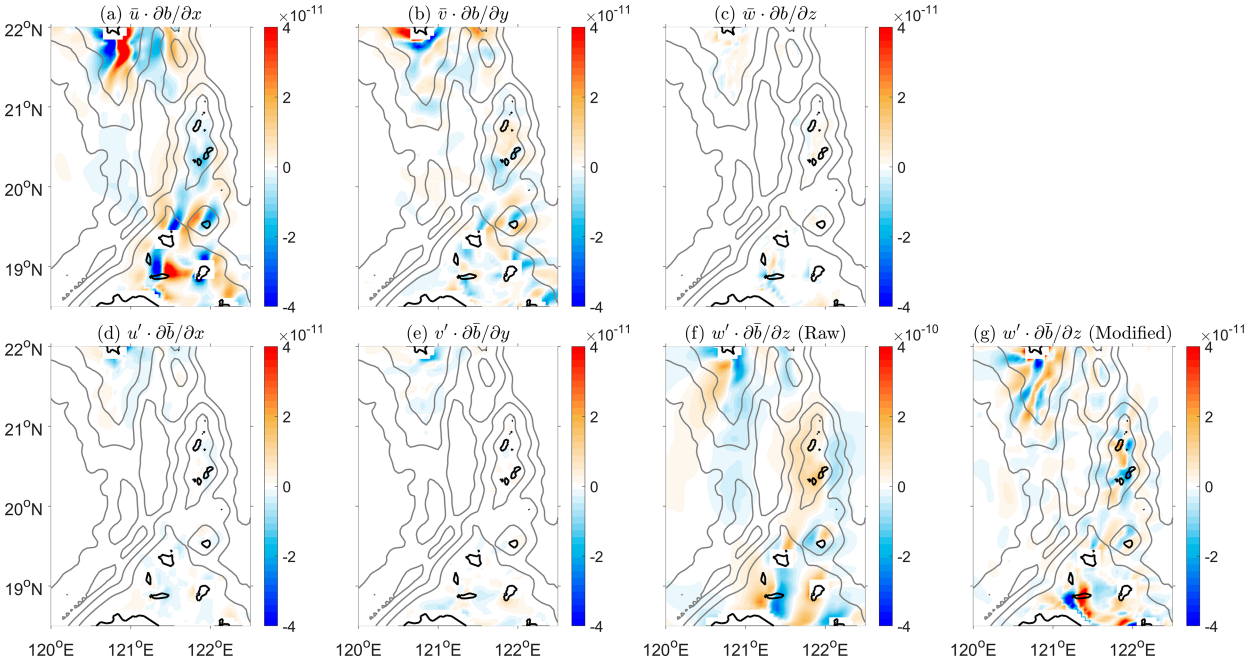

FIG. 9. (a)–(g) Time–depth-averaged values of the six nonlinear terms in Eq. (11). Note that the color bar range of (f) is different from the others. The gray curves denote the 1000-, 2000-, and 3000-m isobaths. The values shown in (g) are the same as those in (f) but remove the contribution of oceanic background stratification.

Figs. 12c and 12d. Because the initial locations and settings of these rays are the same in the two months, the different tracks of these rays are caused by the different phase speeds (Figs. 12c,d). According to the Taylor–Goldstein equation,

$$\frac{d^2\widetilde{W}}{dz^2}+\left[\frac{N^2}{(\widetilde{U}-c)^2}-|k|^2-\frac{1}{\widetilde{U}-c}\frac{d^2\widetilde{U}}{dz^2}\right]\widetilde{W}=0, \tag{33}$$

and the relationship between phase speed and eigenspeed

$$c_p=\frac{\omega}{\sqrt{\omega^2-f^2}}c, \tag{34}$$

where $\widetilde{W}$ is the vertical velocity eigenfunction, c is the eigenspeed, N is the buoyancy frequency, $\widetilde{U}$ is the background currents, k is the horizontal wavenumber, c_p is the phase speed, ω is the M_2 IT frequency, and f is the local Coriolis frequency; both the KC's velocity $\widetilde{U}$ and stratification N can modulate the M_2 IT phase speed. Further analysis indicates that the

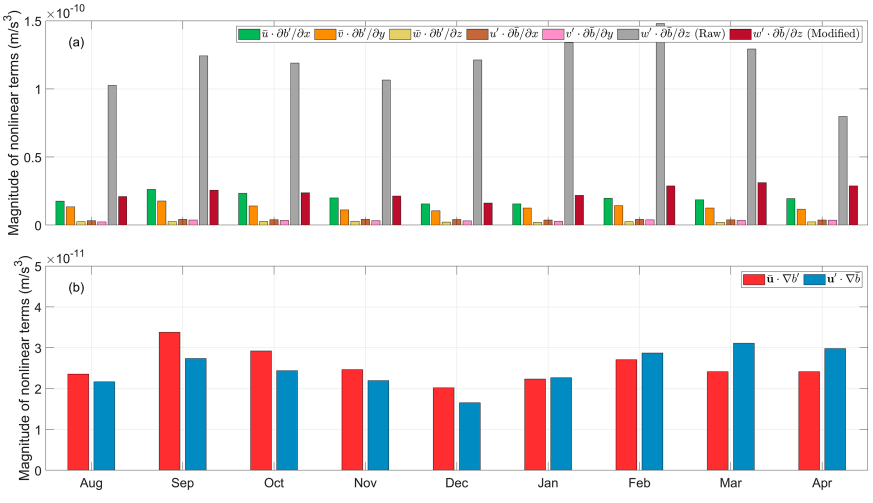

FIG. 10. Domain–time–depth-averaged magnitude of (a) the six nonlinear terms and (b) $\bar{\mathbf{u}}\cdot\nabla b'$ and $\mathbf{u}'\cdot\nabla\bar{b}$ in Eq. (11) for each month. Note that the contribution of oceanic background stratification has been removed for the results shown in (b).

FIG. 11. Sensitivities of zonal energy flux to the pressure perturbation (ΔF_P^x; blue), zonal baroclinic tidal currents (ΔF_U^x; red), and their phase difference ($-\Delta F_\theta^x$; green) integrated along the (a) west and (b) east boundaries of the LS.

KC's velocity plays a more important role than the stratification in determining the M_2 IT phase speed (not shown), which is consistent with previous studies (Buijsman et al. 2017; Xu et al. 2021; Cao et al. 2022).

5. Discussion and summary

Based on the interaction theory between subtidal motions and ITs as well as 9-month numerical simulation results, this study investigates the modulation of the KC on the M_2 IT

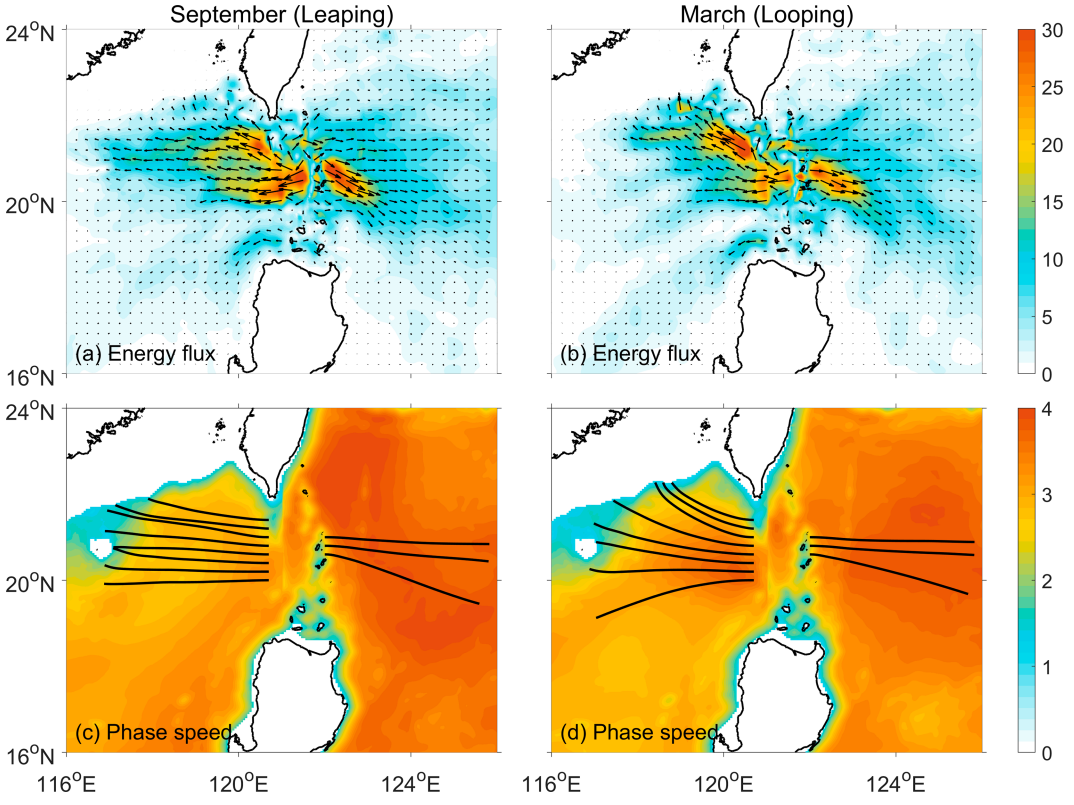

FIG. 12. The M_2 energy flux (magnitude: shading; kW m^{-1}; direction: black quivers) averaged in (a) September 2010 and (b) March 2011. The M_2 phase speeds (shading; m s^{-1}) in (c) September 2010 and (d) March 2011. The black curves denote the ray-tracing results based on the model developed by Duda et al. (2018).

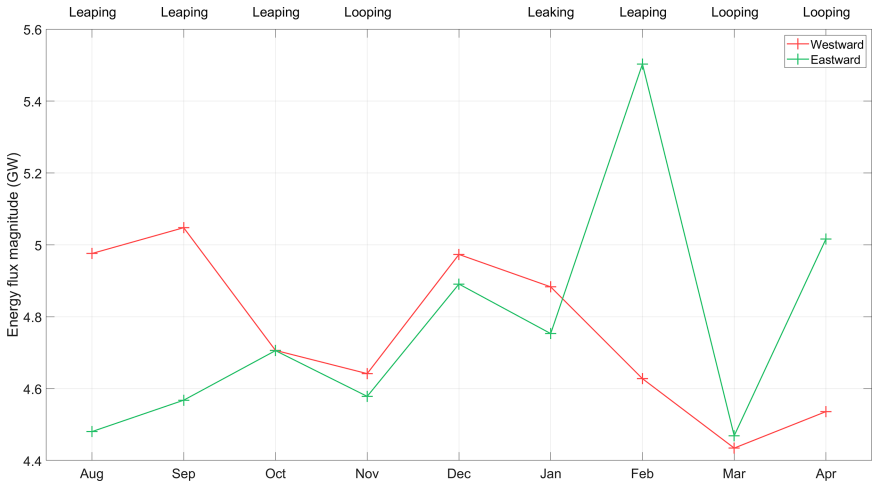

FIG. 13. Magnitude of the westward (red) and eastward (green) M_2 IT energy fluxes radiated from the LS in each month.

energetics at the LS and evaluates the contributions of the KC's velocity and stratification to the modulation.

First, in addition to the tidal conversion, the KC's stratification dominates the energy source terms in the IT energy budget and fuels the generation of the M_2 ITs. Actually, the KC can directly modulate the IT energy budget through buoyancy production, shear production, and advection. Among them, buoyancy production is associated with the KC's stratification, while shear production and advection are related to the KC's velocity. The result indicates that the magnitude of buoyancy production exceeds that of both shear production and advection individually, as well as their combined total, regardless of the path taken by the KC. Furthermore, the sum of buoyancy production, shear production, and advection is positive, demonstrating that the KC tends to enhance the M_2 IT energy at the LS.

Second, the KC's velocity dominates the variabilities of phase speed and energy flux, thus determining the scattering of the M_2 ITs. Solutions of the Taylor–Goldstein equation indicate that the KC's velocity plays a more important role than the stratification in determining the eigenspeed and hence the phase speed of the M_2 ITs, which is consistent with previous studies (Buijsman et al. 2017; Xu et al. 2021; Cao et al. 2022). In other words, the KC's velocity contributes more than the stratification to modulating the propagation of the M_2 ITs. Consequently, the energy flux of the M_2 ITs exhibits significant variabilities, in response to different KC paths. Moreover, sensitivity analysis indicates that the baroclinic tidal currents play a more important role than the pressure perturbation in determining the M_2 IT energy flux, which is modulated by the KC's velocity.

We also examined the sensitivity of the M_2 tidal conversion at the LS and found that the bottom pressure perturbation plays a dominant role. This finding is different from Kerry et al. (2014a) who showed that the phase difference between bottom pressure perturbation and vertical barotropic velocity is more important than the bottom pressure perturbation in the tidal conversion variability. Through a comprehensive comparison between this study and Kerry et al. (2014a), we speculate that this difference is related to the different simulation domain. In Kerry et al. (2014a), the simulation domain contained the Mariana Island Arc, and the M_2 ITs at the LS are affected by those radiated from the Mariana Island Arc (Kerry et al. 2013). As demonstrated by Kelly and Nash (2010), the remotely generated shoaling ITs can change the local pressure perturbation and modulate the tidal conversion. Kerry et al. (2014a) also mentioned that considering the ITs radiated from the Mariana Island Arc, the M_2 tidal conversion variability at the LS became 1.3 times larger.

Results of this study also show that under the influence of the KC, the magnitude and spatial pattern of the M_2 energy flux radiating from the LS into the South China Sea exhibit greater variability than those of the M_2 energy flux into the Philippine Sea (Figs. 11 and 12). This explains, to some extent, the larger incoherence of semidiurnal ITs in the South China Sea compared to the Philippine Sea (Kerry et al. 2016; Cao et al. 2017, 2022). Our analysis further reveals that the KC's velocity contributes more than its stratification to the variability of both magnitude and spatial pattern of the M_2 energy flux. This is also consistent with the findings of Buijsman et al. (2017) and Cao et al. (2022) that the subtidal motion's velocity plays a more important role than its stratification in causing IT incoherence. In other words, a relationship exists between the subtidal motion's velocity and IT incoherence. Establishing this relationship would advance our understanding of IT incoherence and variability of IT-induced turbulent mixing, as incoherent ITs have been demonstrated to have a larger proportion of higher modes and cause stronger shear than coherent ITs (e.g., Liu et al. 2016; Cao et al. 2019).

Previous studies demonstrated that the generation, propagation, dissipation, and incoherence of ITs near the LS are affected by the KC, especially when it takes different paths (e.g., Kerry et al. 2014a, 2016; Xu et al. 2021; Cao et al. 2022). In our simulations, the averaged tidal conversion (20.61 GW) and energy flux divergence (10.62 GW) of the M_2 ITs at the

LS under the leaping KC are greater than those (20.23 GW for tidal conversion and 10.08 GW for energy flux divergence) under the looping KC, which is consistent with the finding of Xu et al. (2021). However, for specific months, the aforementioned conclusion may be invalid. For example, the M_2 tidal conversion in August 2010 (19.59 GW) when the KC took a leaping path is smaller than that in April 2011 (21.06 GW) when the KC took a looping path. This is because, in addition to the KC path, there also exist other influencing factors, such as the intensity of the KC (e.g., Jan et al. 2012) and variability of ocean background stratification (e.g., Guo et al. 2020, 2024).

Based on the analysis of 24-yr satellite altimetry sea surface height data, Zhao and Qiu (2023) reported the seasonal west–east seesaw of the M_2 IT energy flux at the LS. To be specific, the westward M_2 IT energy flux is stronger in summer (July–September) and fall (October–December), whereas the eastward M_2 IT energy flux is stronger in winter (January–March) and spring (April–June). This seasonal seesaw phenomenon is generally reproduced in this study (Fig. 13). Zhao and Qiu (2023) suggested that the seasonal seesaw phenomenon is mainly determined by the ocean stratification and the KC. However, the correlation between the seasonal seesaw phenomenon and the KC is not clearly illustrated by our simulations (Fig. 13). Actually, this seasonal seesaw phenomenon is also reproduced by Guo et al. (2020). In their model configurations, only the horizontally homogeneous stratification in winter and summer is used and no background currents are considered. According to these results, we speculate that the seasonal variability of ocean background stratification, which results in different interference patterns of the M_2 ITs at the LS (Alford et al. 2011; Buijsman et al. 2012, 2014; Guo et al. 2020), is the major cause of the seasonal seesaw of the M_2 ITs at the LS. To further validate this speculation, longer simulations will be conducted in the future.

Acknowledgments. The authors deeply thank the editor and reviewers for their constructive suggestions that greatly improved the manuscript. This study is supported by the National Natural Science Foundation of China (Grant 42176002) and the Fundamental Research Funds for the Central Universities (Grant 226-2025-00150). Anzhou Cao acknowledges the funding of ZJU Tang Scholar. Xinyu Guo is supported by Grants in Aid for Scientific Research (MEXT KAKENHI Grant 22H05206). This study is also supported by the Ministry of Education, Culture, Sports, Science and Technology (MEXT), Japan, to a project on Joint Usage/Research Center–Leading Academia in Marine and Environmental Pollution Research (Lamer). The authors also thank Dr. Shuya Wang for constructive discussions.

Data availability statement. The CROCO code and tidal forcing data are available at https://www.croco-ocean.org/download/. The HYCOM reanalysis data are available at https://tds.hycom.org/thredds/catalogs/GLBv0.08/expt_53.X.html. The surface forcing data are available at https://tds.hycom.org/thredds/catalog/datasets/force/ncep_cfsr/netcdf/catalog.html and https://tds.hycom.org/thredds/catalog/datasets/force/ncep_cfsv2/netcdf/catalog.html. The satellite-observed surface geostrophic currents are available at https://data.marine.copernicus.eu/product/SEALEVEL_GLO_PHY_CLIMATE_L4_MY_008_057/services. The data shown in the figures of this study are available at https://doi.org/10.5281/zenodo.15161777.

REFERENCES

Alford, M. H., and Coauthors, 2011: Energy flux and dissipation in Luzon Strait: Two tales of two ridges. *J. Phys. Oceanogr.*, **41**, 2211–2222, https://doi.org/10.1175/JPO-D-11-073.1.

——, and Coauthors, 2015: The formation and fate of internal waves in the South China Sea. *Nature*, **521**, 65–69, https://doi.org/10.1038/nature14399.

Bell, T. H., 1975: Lee waves in stratified flows with simple harmonic time dependence. *J. Fluid Mech.*, **67**, 705–722, https://doi.org/10.1017/S0022112075000560+.

Buijsman, M. C., S. Legg, and J. Klymak, 2012: Double-ridge internal tide interference and its effect on dissipation in Luzon Strait. *J. Phys. Oceanogr.*, **42**, 1337–1356, https://doi.org/10.1175/JPO-D-11-0210.1.

——, and Coauthors, 2014: Three-dimensional double-ridge internal tide resonance in Luzon Strait. *J. Phys. Oceanogr.*, **44**, 850–869, https://doi.org/10.1175/JPO-D-13-024.1.

——, B. K. Arbic, J. G. Richman, J. F. Shriver, A. J. Wallcraft, and L. Zamudio, 2017: Semidiurnal internal tide incoherence in the equatorial Pacific. *J. Geophys. Res. Oceans*, **122**, 5286–5305, https://doi.org/10.1002/2016JC012590.

Cao, A., Z. Guo, X. Lv, J. Song, and J. Zhang, 2017: Coherent and incoherent features, seasonal behaviors and spatial variations of internal tides in the northern South China Sea. *J. Mar. Syst.*, **172**, 75–83, https://doi.org/10.1016/j.jmarsys.2017.03.005.

——, ——, S. Wang, X. Chen, X. Lv, and J. Song, 2019: Upper ocean shear in the northern South China Sea. *J. Oceanogr.*, **75**, 525–539, https://doi.org/10.1007/s10872-019-00520-x.

——, ——, ——, X. Guo, and J. Song, 2022: Incoherence of the M_2 and K_1 internal tides radiated from the Luzon Strait under the influence of looping and leaping Kuroshio. *Prog. Oceanogr.*, **206**, 102850, https://doi.org/10.1016/j.pocean.2022.102850.

——, ——, ——, X. Chen, J. Song, and X. Guo, 2023: Energetics of the M_2 internal tides modulated by typhoons at the Luzon Strait. *Ocean Modell.*, **186**, 102243, https://doi.org/10.1016/j.ocemod.2023.102243.

——, ——, X. Chen, X. Guo, and J. Song, 2025: Interaction between the M_2 internal tides and typhoon-induced near-inertial waves near the Luzon Strait. *Deep-Sea Res. I*, **217**, 104452, https://doi.org/10.1016/j.dsr.2025.104452.

Carter, G. S., O. B. Fringer, and E. D. Zaron, 2012: Regional models of internal tides. *Oceanography*, **25** (2), 56–65, https://doi.org/10.5670/oceanog.2012.42.

Duda, T. F., Y.-T. Lin, M. Buijsman, and A. E. Newhall, 2018: Internal tidal modal ray refraction and energy ducting in baroclinic Gulf Stream currents. *J. Phys. Oceanogr.*, **48**, 1969–1993, https://doi.org/10.1175/JPO-D-18-0031.1.

Dunphy, M., and K. G. Lamb, 2014: Focusing and vertical mode scattering of the first mode internal tide by mesoscale eddy interaction. *J. Geophys. Res. Oceans*, **119**, 523–536, https://doi.org/10.1002/2013JC009293.

Egbert, G. D., and S. Y. Erofeeva, 2002: Efficient inverse modeling of barotropic ocean tides. *J. Atmos. Oceanic Technol.*, **19**,

183–204, https://doi.org/10.1175/1520-0426(2002)019<0183:EIMOBO>2.0.CO;2.

Guo, Z., A. Cao, X. Lv, and J. Song, 2020: Impacts of stratification variation on the M_2 internal tide generation in Luzon Strait. *Atmos. Ocean*, **58**, 206–218, https://doi.org/10.1080/07055900.2020.1767534.

——, S. Wang, A. Cao, J. Xie, J. Song, and X. Guo, 2023: Refraction of the M_2 internal tides by mesoscale eddies in the South China Sea. *Deep-Sea Res. I*, **192**, 103946, https://doi.org/10.1016/j.dsr.2022.103946.

——, ——, ——, X. Chen, J. Song, and X. Guo, 2024: Variability of the M_2 internal tides in the Luzon Strait under climate change. *Climate Dyn.*, **62**, 5019–5028, https://doi.org/10.1007/s00382-024-07148-8.

Hazewinkel, J., and K. B. Winters, 2011: PSI of the internal tide on a β plane: Flux divergence and near-inertial wave propagation. *J. Phys. Oceanogr.*, **41**, 1673–1682, https://doi.org/10.1175/2011JPO4605.1.

Jan, S., C.-S. Chern, J. Wang, and M.-D. Chiou, 2012: Generation and propagation of baroclinic tides modified by the Kuroshio in the Luzon Strait. *J. Geophys. Res.*, **117**, C02019, https://doi.org/10.1029/2011JC007229.

Kelly, S. M., and J. D. Nash, 2010: Internal-tide generation and destruction by shoaling internal tides. *Geophys. Res. Lett.*, **37**, L23611, https://doi.org/10.1029/2010GL045598.

——, and P. F. J. Lermusiaux, 2016: Internal-tide interactions with the Gulf Stream and Middle Atlantic Bight shelfbreak front. *J. Geophys. Res. Oceans*, **121**, 6271–6294, https://doi.org/10.1002/2016JC011639.

Kerry, C. G., B. S. Powell, and G. S. Carter, 2013: Effects of remote generation sites on model estimates of M_2 internal tides in the Philippine Sea. *J. Phys. Oceanogr.*, **43**, 187–204, https://doi.org/10.1175/JPO-D-12-081.1.

——, ——, and ——, 2014a: The impact of subtidal circulation on internal tide generation and propagation in the Philippine Sea. *J. Phys. Oceanogr.*, **44**, 1386–1405, https://doi.org/10.1175/JPO-D-13-0142.1.

——, ——, and ——, 2014b: The impact of subtidal circulation on internal-tide-induced mixing in the Philippine Sea. *J. Phys. Oceanogr.*, **44**, 3209–3224, https://doi.org/10.1175/JPO-D-13-0249.1.

——, ——, and ——, 2016: Quantifying the incoherent M_2 internal tide in the Philippine Sea. *J. Phys. Oceanogr.*, **46**, 2483–2491, https://doi.org/10.1175/JPO-D-16-0023.1.

Liu, Q., X. Xie, X. Shang, and G. Chen, 2016: Coherent and incoherent internal tides in the southern South China Sea. *Chin. J. Oceanol. Limnol.*, **34**, 1374–1382, https://doi.org/10.1007/s00343-016-5171-5.

Löb, J., J. Köhler, C. Mertens, M. Walter, Z. Li, J. von Storch, Z. Zhao, and M. Rhein, 2020: Observations of the low-mode internal tide and its interaction with mesoscale flow south of the Azores. *J. Geophys. Res. Oceans*, **125**, e2019JC015879, https://doi.org/10.1029/2019JC015879.

Munk, W., and C. Wunsch, 1998: Abyssal recipes II: Energetics of tidal and wind mixing. *Deep-Sea Res. I*, **45**, 1977–2010, https://doi.org/10.1016/S0967-0637(98)00070-3.

Müller, M., 2013: On the space- and time-dependence of barotropic-to-baroclinic tidal energy conversion. *Ocean Modell.*, **72**, 242–252, https://doi.org/10.1016/j.ocemod.2013.09.007.

——, J. Y. Cherniawsky, M. G. G. Foreman, and J.-S. von Storch, 2012: Global M_2 internal tide and its seasonal variability from high resolution ocean circulation and tide modeling. *Geophys. Res. Lett.*, **39**, L19607, https://doi.org/10.1029/2012GL053320.

Nan, F., H. Xue, F. Chai, L. Shi, M. Shi, and P. Guo, 2011: Identification of different types of Kuroshio intrusion into the South China Sea. *Ocean Dyn.*, **61**, 1291–1304, https://doi.org/10.1007/s10236-011-0426-3.

Niwa, Y., and T. Hibiya, 2011: Estimation of baroclinic tide energy available for deep ocean mixing based on three-dimensional global numerical simulations. *J. Oceanogr.*, **67**, 493–502, https://doi.org/10.1007/s10872-011-0052-1.

——, and ——, 2014: Generation of baroclinic tide energy in a global three-dimensional numerical model with different spatial grid resolutions. *Ocean Modell.*, **80**, 59–73, https://doi.org/10.1016/j.ocemod.2014.05.003.

Pawlowicz, R., B. Beardsley, and S. Lentz, 2002: Classical tidal harmonic analysis including error estimates in MATLAB using T_TIDE. *Comput. Geosci.*, **28**, 929–937, https://doi.org/10.1016/S0098-3004(02)00013-4.

Rudnick, D. L., and Coauthors, 2003: From tides to mixing along the Hawaiian Ridge. *Science*, **301**, 355–357, https://doi.org/10.1126/science.1085837.

Savage, A. C., A. F. Waterhouse, and S. M. Kelly, 2020: Internal tide nonstationarity and wave–mesoscale interactions in the Tasman Sea. *J. Phys. Oceanogr.*, **50**, 2931–2951, https://doi.org/10.1175/JPO-D-19-0283.1.

Simmons, H. L., R. W. Hallberg, and B. K. Arbic II, 2004: Internal wave generation in a global baroclinic tide model. *Deep-Sea Res.*, **51**, 3043–3068, https://doi.org/10.1016/j.dsr2.2004.09.015.

Smith, S. G. L., and W. R. Young, 2003: Tidal conversion at a very steep ridge. *J. Fluid Mech.*, **495**, 175–191, https://doi.org/10.1017/S0022112003006098.

Wang, S., A. Cao, X. Chen, Q. Li, and J. Song, 2021: On the resonant triad interaction over mid-ocean ridges. *Ocean Modell.*, **158**, 101734, https://doi.org/10.1016/j.ocemod.2020.101734.

Xu, Z., Y. Wang, Z. Liu, J. C. McWilliams, and J. Gan, 2021: Insight into the dynamics of the radiating internal tide associated with the Kuroshio Current. *J. Geophys. Res. Oceans*, **126**, e2020JC017018, https://doi.org/10.1029/2020JC017018.

Zhao, Z., 2019: Mapping internal tides from satellite altimetry without blind directions. *J. Geophys. Res. Oceans*, **124**, 8605–8625, https://doi.org/10.1029/2019JC015507.

——, 2024: Internal tides from SWOT: A 75-day instantaneous mode-1 M_2 internal tide model. *J. Geophys. Res. Oceans*, **129**, e2024JC021174, https://doi.org/10.1029/2024JC021174.

——, and B. Qiu, 2023: Seasonal west-east seesaw of M_2 internal tides from the Luzon Strait. *J. Geophys. Res. Oceans*, **128**, e2022JC019281, https://doi.org/10.1029/2022JC019281.

——, M. H. Alford, J. A. MacKinnon, and R. Pinkel, 2010: Long-range propagation of the semidiurnal internal tide from the Hawaiian Ridge. *J. Phys. Oceanogr.*, **40**, 713–736, https://doi.org/10.1175/2009JPO4207.1.